Composites Science and Technology 89 (2013) 202–210

Contents lists available at ScienceDirect

Composites Science and Technology

journal homepage: www.elsevier.com/locate/compscitech

Finding fibres and their contacts within 3D images of disordered fibrous media

J. Viguié [a,b,c,d], P. Latil [a,b,c,d], L. Orgéas [a,b,*], P.J.J. Dumont [c,d], S. Rolland du Roscoat [a,b,e], J.-F. Bloch [c,d], C. Marulier [a,b,c,d], O. Guiraud [a,b,c,d]

[a] CNRS, 3SR Lab., BP 53, 38041 Grenoble Cedex 9, France
[b] Université de Grenoble Alpes, 3SR Lab., BP 53, 38041 Grenoble Cedex 9, France
[c] CNRS, LGP2, CS 10065, 38402 Saint-Martin-d'Hères, France
[d] Université de Grenoble Alpes, LGP2, CS 10065, 38402 Saint-Martin-d'Hères, France
[e] ESRF, ID 19 Topography and Microtomography Group, 38043 Grenoble Cedex, France

ARTICLE INFO

Article history:
Received 16 July 2013
Received in revised form 25 September 2013
Accepted 28 September 2013
Available online 15 October 2013

Keywords:
A. Fibres
A. Polymer–matrix composites (PMCs)
D. Non-destructive testing
D. Microtomography

ABSTRACT

Modelling physical and mechanical properties of fibrous materials requires a relevant description of their microstructures, *e.g.* the descriptors of fibres and fibre–fibre contacts. In this work, a method is proposed to identify fibres with complex cross sections and their contacts from 3D images of disordered fibrous media, obtained from X-ray microtomography. The image analysis procedure first consists in obtaining a map of the local fibre orientation. Fibres are then detected by deleting regions of high local orientation gradients. Therewith, dilatation operations using slender orientated structuring elements are performed to retrieve deleted fibre parts. The procedure thus provides 3D images with labelled fibres and fibre–fibre contacts. Its relevance is assessed by analysing the microstructures of three typical fibrous media used in short fibre reinforced polymer composites or as paper materials: mats of (i) mono-disperse copper fibres with circular cross sections, (ii) glass fibres bundles, (iii) wood fibres.

1. Introduction

Fibrous materials are of great interest as their physical and mechanical properties can be tailored by tuning the nature, content, geometry, orientation and position of fibres, as well as by changing the morphology or the nature of contacts between fibres. However, the full potential of fibrous materials such as fibre reinforced polymer composites or papers is still not completely exploited because the relations between their fibrous microstructure, the mechanical or physical micro-mechanisms activated at the fibre scale and their macroscale behaviour often remain misunderstood.

X-ray microtomography images are very useful to obtain 3D and appropriate descriptions of the complex microstructures of fibrous materials and their evolutions under varying physical loading conditions. For instance, the measurement of microstructure parameters such as porosity, specific surface or mean chord lengths can provide some relevant information on the global evolution of fibrous microstructures during physical or mechanical loadings [4,18]. Such analyses can be refined by measuring kinematic fields using digital image correlation [7,23]. However, to finely analyse fibre scale mechanisms at the fibre scale, additional information covering the positions, orientations, geometries of the fibre centrelines and of the fibre–fibre contacts must be extracted from the 3D micrographs [9,13,14,16]. As a first requirement to achieve this, one has to recognise, automatically if possible, fibres and fibre–fibre contacts. This is still problematic.

To date, several methods have been investigated. One of them consists in extracting the geometrical fibrous skeleton by using homotopic thinning algorithm [11,15,21,26]. Once the skeleton is extracted, the principal branches are identified by classifying the skeleton voxels into branches and nodes and by merging branches with the most similar orientation [11]. In the special case of mono-disperse fibres with circular cross sections, another method consists in extracting principal branches by using threshold operations on the distance (transform) map before applying the homotopic thinning algorithm [17].

Once the principal branches are extracted, the final labelled image can be obtained by dilation of the segmented skeleton inside the original image [11,12] or by reconstructing volumes from CAD operations, if possible [17]. However, skeletonization methods are often restricted to low fibre contents and to fibres exhibiting sufficiently simple and isotropic cross sections from a geometrical standpoint.

* Corresponding author at: CNRS, 3SR Lab., BP 53, 38041 Grenoble Cedex 9, France. Tel.: +33 476827073.
E-mail address: laurent.orgeas@3sr-grenoble.fr (L. Orgéas).

0266-3538/$ - see front matter © 2013 Elsevier Ltd. All rights reserved.
http://dx.doi.org/10.1016/j.compscitech.2013.09.023

Another largely investigated method consists in tracking fibres by following the centre of mass of the fibre cross sections (see for example Latil et al. [9] in the case of a bundle of aligned fibres) or the centre of lumens in the case of wood hollow fibres [20]. This method necessitates the recognition of the fibre cross sections from 2D or 3D images [24,25,13]. In the case of wood fibres, another method uses the Radon transform to find the position and the orientation of the fibre wall [2].

However, the recognition and the tracking of fibres with more complex cross sections remain a very tough task using the above methods. Instead, methods based on the use of local fibre orientation maps provide some relevant information to overcome this challenging issue. Such maps can be obtained by several methods, applied on binarised or grey level images, as the chord length (transform) maps [5,19], the anisotropic Gaussian orientation space or by using the inertia moments of directional distance maps. The latter has the advantage of inspecting a limited number of directions [3,1,8]. Doing so, Altendorf and Jeulin [1] identified cylindrical fibres inside fibrous networks by analysing the local fibre radius provided by the local fibre orientation map. Nevertheless, the use of the local fibre radius seems to restrain the analyses to fibres with rather isotropic cross sections.

In this work, we propose a method to identify fibres with more complex and anisotropic cross sections, by further exploiting the information provided by the local fibre orientation map, *i.e.* by analysing finely the variations of the local fibre orientation. Fibres are detected by deleting regions of high misorientation, as these zones correspond to the vicinities of fibre–fibre contacts. To retrieve the removed fibre parts, dilatation operations using slender orientated structuring elements are then performed. This finally yields to the labelling and to the characterisation of fibres and fibre–fibre contacts. The method is described in detail in the Section 3. Its relevance is gauged from 3D images of four real fibrous architectures, the fibre geometries of which exhibit increasing complexity (Section 4).

2. Considered fibrous materials

The fibrous architectures of two short fibre reinforced polymer composites and two handmade papers were analysed with the method proposed in the next section. The studied fibrous networks are depicted in the 3D images given in Fig. 1.

- The first fibrous network was composed of conductive copper fibres with circular cross section (diameter of 0.2 mm, length of 10 mm) exhibiting a fibre volume fraction of 0.17 and planar fibre orientation (in the $(\mathbf{e}_1, \mathbf{e}_2)$ plane) with a moderate preferential fibre orientation along the $\mathbf{e}_1$ direction. This sample was investigated in detail in Orgéas et al. [17]. The 3D image (Fig. 1(a)) had a size of $360 \times 360 \times 88$ voxels for a specimen of $6.1 \times 6.1 \times 1.5\ mm^3$, *i.e.* the voxel size was $17^3\ \mu m^3$. As a result, fibres had a cross section diameter of 11.7 voxels. Fibres were detected and counted following the procedure described in Orgéas et al. [17], which consisted in separating contacting fibres by performing a thresholding operation on the 3D Euclidian distance map and detecting the centreline of each individual fibre by applying the homotopic algorithm. $N_f = 133$ fibres were identified. Fibre–fibre contacts were obtained by regenerating numerically fibres from their centrelines [9]. A contact was considered relevant each time a couple of regenerated fibres overlapped: $N_c = 214$ contacts were found.
- The second fibrous media was a network of glass fibre bundles commonly used as reinforcement in Sheet Moulding Compounds (SMC) and Glass or Carbon Mat Thermoplastics (G/CMT). This network was investigated in detail in Guiraud et al. [6]. The bundles had a length of 13 mm and exhibited a planar random orientation: fibre bundles were mostly orientated in the $(\mathbf{e}_1, \mathbf{e}_2)$ plane. The fibre bundle volume fraction was equal to 0.13. Fibre bundles exhibited irregular and flat cross sections, their typical thickness and width were approximately equal to 0.2 mm and 1 mm, respectively. The corresponding 3D image displayed in Fig. 1(b) had a size of $500 \times 500 \times 146$ voxels for a specimen volume of $15.6 \times 15.6 \times 4.5\ mm^3$, *i.e.* the voxel size was $31.2^3\ \mu m^3$. As a result, the cross sections of bundles had typical thicknesses and widths of 3 and 15 voxels, respectively. The bundle centrelines were manually detected [10,6]. A number $N_f = 148$ bundles was determined. To estimate the number of bundle-bundle contacts, Guiraud et al. [6] regenerated numerically the bundles from their centrelines by assuming that their cross sections were elliptical, constant with major axes orientated along the $(\mathbf{e}_1, \mathbf{e}_2)$ plane. $N_c = 116$ contacts were found.
- The third studied material (see Fig. 1(c)) was a network of cellulosic (wood pulp) fibres obtained by laboratory papermaking operations using low pressing conditions [14] to obtain a final basis weight of $40\ g\ m^{-2}$. The fibre length was about 1 mm to 2–3 mm. Fibres were mostly orientated in the $(\mathbf{e}_1, \mathbf{e}_2)$ plane. The fibre volume fraction was close to 0.15. Their cross sections were irregular, rather flat but exhibited pronounced twist along the fibre centrelines. Their minimal thickness was around 5 μm and their mean maximal width was close to 33 μm [14]. Notice that some of the fibres exhibited some hollow cross sections, which corresponds to fibres with partially opened lumens. The 3D image had a size of $300 \times 300 \times 200$ voxels for a specimen volume of $210 \times 210 \times 140\ \mu m^3$, *i.e.* the voxel size was $0.7^3\ \mu m^3$. Hence, the minimal fibre thickness was higher than 7 voxels.
- The fourth studied material (see Fig. 1(d)) was also a network of cellulosic (wood pulp) fibres obtained by a laboratory papermaking process and standard pressing conditions [14] for a basis weight of $15\ g\ m^{-2}$. The fibres had the same morphological features as those of the previous network. However, due to higher pressing conditions, the maximal widths of the fibre cross sections mostly lay along the $(\mathbf{e}_1, \mathbf{e}_2)$ plane [14]. The 3D image had a size of $450 \times 450 \times 65$ voxels for a specimen volume of $315 \times 315 \times 45\ \mu m^3$, *i.e.* the voxel size was $0.7^3\ \mu m^3$.

3. Description of the method

By analysing data provided from the local fibre orientation map, the proposed method is an extension of the work suggested by Altendorf and Jeulin [1]. Starting from segmented and binarised 3D image, it requires three steps. In step (i), a map of the local fibre orientation is constructed. In step (ii), fibres are separated by detecting regions of high orientation gradients. Dilatation operations using slender orientated structuring elements are finally performed in step (iii) to retrieve the fibre parts deleted during step (ii). This algorithm was implemented in Matlab. It is detailed below:

(i) For each voxel of the fibre phase of spatial position $\mathbf{X}$, the directional Euclidian distance transforms to the non-fibrous phase were first computed [1]. The orthogonal directions $\mathbf{t}_i$ along which the distance map was estimated, corresponded to those given by the n neighbours of the considered voxel. Here, the 26-connex neighbours were taken into account (*i.e.* distributed in a cube of 3 voxels edge length centred on the considered voxel). Moreover, in order to refine the description along the principal orientation plane of the considered fibrous materials, one additional layer of neighbours was considered in the faces of the cube normal to the $\mathbf{e}_1$ or $\mathbf{e}_2$

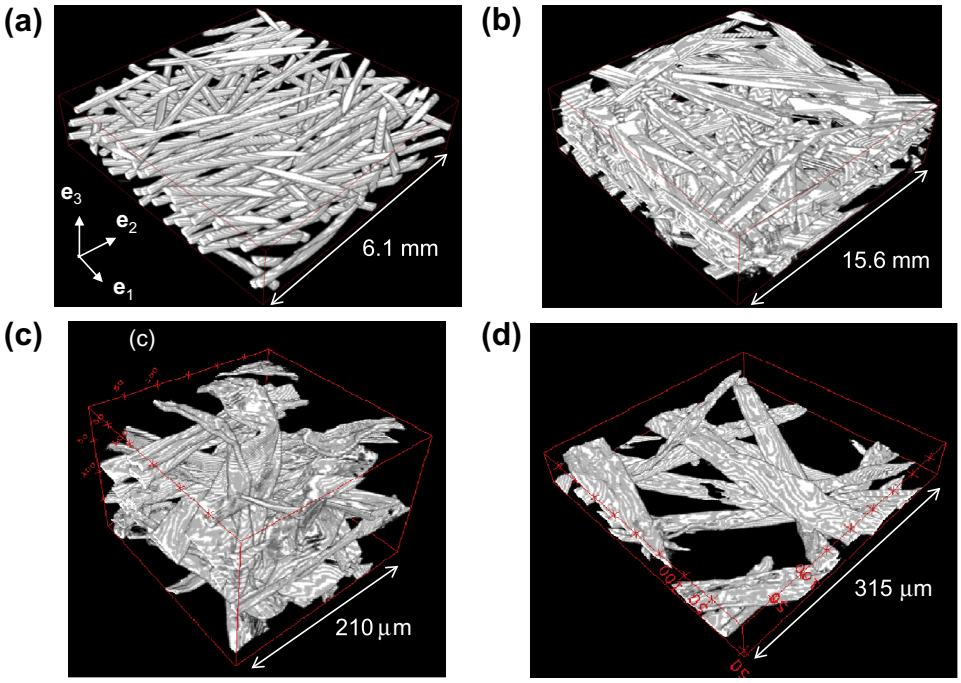

Fig. 1. 3D images obtained by X-ray tomography of (a) a network of copper fibres reinforcing a PMMA polymer matrix (360 × 360 × 88 voxels, 1 voxel = 17^3 µm^3), (b) a network of glass fibre bundles reinforcing a thermoset polyester matrix with mineral fillers (500 × 500 × 146 voxels, 1 voxel = 31.2^3 µm^3) and (c) a network of cellulosic fibres with a basis weight of 40 g m^{-2} obtained by a papermaking process under low pressing conditions (300 × 300 × 200 voxels, 1 voxel = 0.7^3 µm^3) and (d) a network of cellulosic fibres with a basis weight of 15 g m^{-2} obtained by a papermaking process under standard pressing conditions (450 × 450 × 65 voxels, 1 voxel = 0.7^3 µm^3).

directions (*i.e.* the 6-connex neighbouring voxels in the $\mathbf{e}_1$ and $\mathbf{e}_2$ directions of the 26-connex neighbours). As a result, $n = 52$ directions were investigated. Notice that such a spatial refinement could be achieved around the whole set of the first 26-connex neighbours without any difficulty in the case of fibrous materials that display no preferred fibre orientation. Then, the distance $\delta(\mathbf{t}_i)$ between the voxel and the non-fibrous phase was calculated, allowing the estimation of the local distance vector $\mathbf{p}_i = d_i\,\mathbf{t}_i$, where $d_i = (\delta(\mathbf{t}_i) + \delta(-\mathbf{t}_i))/2$ is the local mean chord length along $\mathbf{t}_i$. The vectors $\mathbf{p}_i$ were then used to compute the second order local orientation tensor:

$$\mathbf{A} = \frac{1}{n}\sum_{i=1}^{n} \mathbf{p}_i \otimes \mathbf{p}_i. \tag{1}$$

Its principal directions and values are noted $\mathbf{t}_I$, $\mathbf{t}_{II}$, $\mathbf{t}_{III}$ and d_I, d_{II}, d_{III}, respectively. Principal directions were represented by introducing both the orientation angles θ_I, θ_{II} and θ_{III} of the projections of $\mathbf{t}_I$, $\mathbf{t}_{II}$, $\mathbf{t}_{III}$, respectively, in the $(\mathbf{e}_1, \mathbf{e}_2)$ plane with respect to $\mathbf{e}_1$, and the orientation angles ψ_I, ψ_{II} and ψ_{III} of the projections of $\mathbf{t}_I$, $\mathbf{t}_{II}$, $\mathbf{t}_{III}$, respectively, in the $(\mathbf{e}_1, \mathbf{e}_3)$ plane with respect to $\mathbf{e}_1$. To illustrate the evolution of these parameters inside a fibrous medium, Fig. 2 gives 2D maps of their values within a 3D zone extracted from the volume of Fig. 1(b). From this figure, it is worth noting that regions close to a contact between fibres are systematically related to high gradients (i) of the local fibre orientation angle (here only sharp variations of θ_I are observed, since fibres are mostly orientated in the $(\mathbf{e}_1, \mathbf{e}_2)$ plane) and (ii) of the eigenvalues related to the two other perpendicular principal directions (d_{II} and d_{III}). It is also interesting to note that the gradients recorded in the case of the θ_I map are sharper than those observed for the d_{II} or d_{III} ones, which are spread in larger zones around the contact interface. This yields to consider in the following the first principal direction θ_I as the most relevant parameter to identify contact surfaces.

(ii) In order to identify such particular zones, the mean local angular deviation C_p between the first principal local orientation vector $\mathbf{t}_I(\mathbf{X})$ and the first principal local orientation vectors of its n neighbours $\mathbf{t}_I(\mathbf{X} + d\mathbf{X}_i)$ was calculated:

$$C_p(\mathbf{X}) = \frac{1}{n}\sum_{i=1}^{n} |\mathbf{t}_I(\mathbf{X}) \cdot \mathbf{t}_I(\mathbf{X} + d\mathbf{X}_i)|. \tag{2}$$

In the case of the glass fibre bundle network displayed in Fig. 3(a), the resulting map of C_p is depicted in Fig. 3(b). This image highlights obvious differences between contact zones and most of the rest of fibres. Thus, to disconnect contacting fibres with different mean orientations, a segmentation operation using an appropriate threshold of C_p could be achieved. For the considered fibrous materials, typical threshold values of C_p ranging between 0.9 and 1 produced proper segmentations, *i.e.* that could both preserve most of the portions of fibres outside contacting zones and separate contacting fibres (as depicted in Fig. 3(c)).

Then all the 26-connex voxels were grouped and labelled. At this step, some "small" fibre portions were disconnected from the fibre they belonged to. If these volumes were lower than an arbitrary minimum number of voxels (typical user-defined values ranging from 500 to 2000 voxels were here chosen), these small volumes were deleted. They were easily retrieved during the next dilatation operation (iii, see below), together with the small volumes deleted by global C_p thresholding (*cf.* Fig. 3(c)). Thereafter, 90% of labels corresponded to individual fibres. For the remaining 10%, two problems were identified: either some contacting fibres were not well separated or individual "large" portions that should belong to the same fibre were disconnected. To treat these two cases, the threshold value of C_p was reconsidered for the concerned

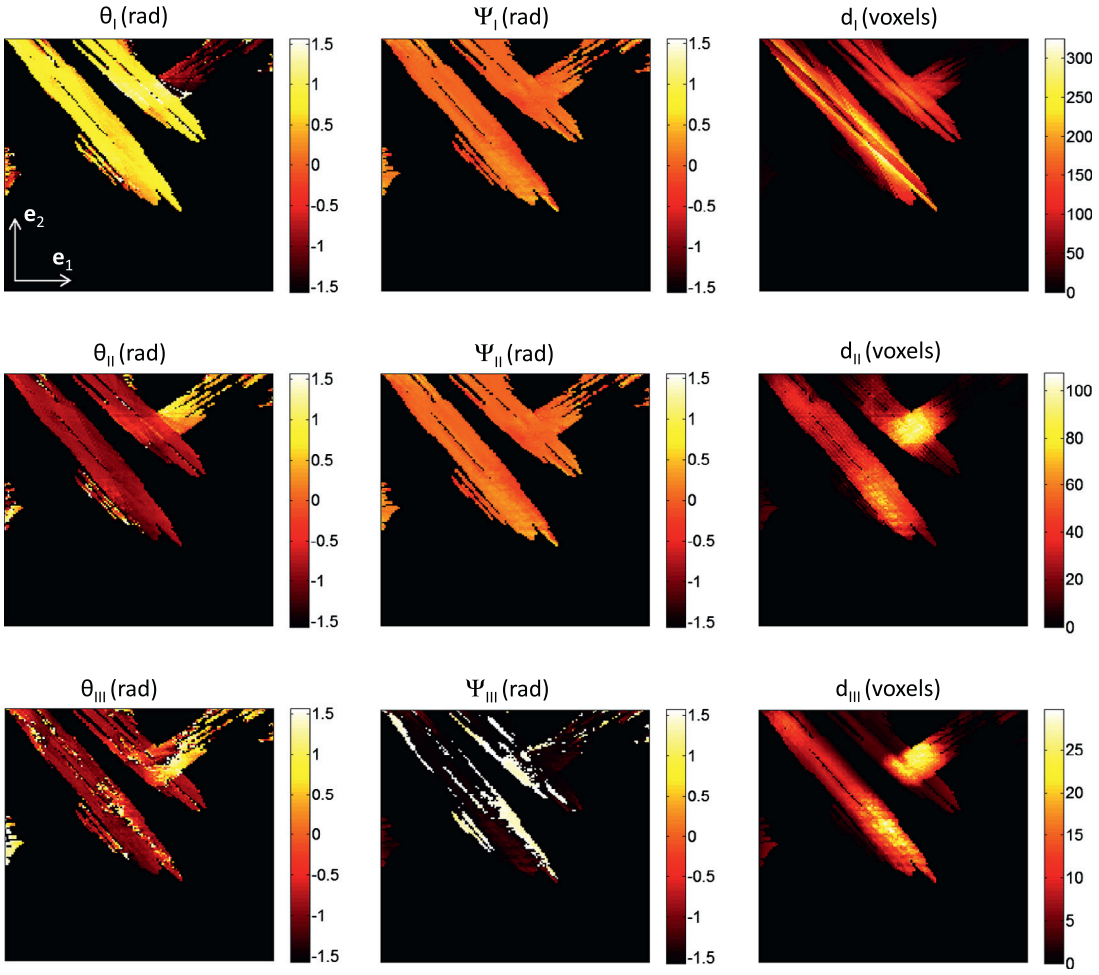

Fig. 2. Maps of the orientation angles θ_I, θ_{II} and θ_{III} and of the projections of the principal directions in the ($\mathbf{e}_1$, $\mathbf{e}_2$) plane with respect to $\mathbf{e}_1$, of the orientation angles Ψ_I, Ψ_{II} and Ψ_{III} of the projections of the principal directions in the ($\mathbf{e}_1$, $\mathbf{e}_3$) plane with respect to $\mathbf{e}_1$, and of the eigenvalues d_I, d_{II} and d_{III}, along the ($\mathbf{e}_1$, $\mathbf{e}_2$) plane of a small segmented 3D image extracted from the volume shown in Fig. 1(b) ($160 \times 160 \times 100$ voxels, 1 voxel = 18^3 μm^3).

labels (*i.e.* "locally"), in order either to separate not well-separated fibres or to reconnect individual portions that should belong to the same fibre. At this stage, an estimation of the total number of fibres N_f was obtained.

It is important to notice that the proposed individualisation method is exclusively based on the detection of the local orientation angle variations. As a result, it does not enable one to detect (nearly) parallel fibres. In the particular cases where parallel fibres could not be separated, the as-treated volumes were subjected to an additional and successful thresholding operation using the distance transform map, as already proposed in Orgéas et al. [17].

(iii) At the end of step (ii), some voxels of the initial fibrous phase were not attributed to labelled fibres (see Fig. 3(c)). To associate them with a proper label, each labelled fibre was subjected to a dilatation using an anisotropic slender structuring element. In the case of the tested fibrous media for which the fibre centrelines were weakly wavy, it was possible to ascribe the mean orientation of the considered fibre to the element orientation, *i.e.* the mean value of the $\mathbf{t}_I$'s within the considered segmented fibre. However, this is not a restriction of the proposed method: for more tortuous fibres, the structuring element could be aligned with the local direction of the $\mathbf{t}_I$'s. The structuring element was defined as a column of one voxel thick with a length similar to the characterisitic fibre width. The dilatation was restricted to the fibrous phase of the initial image. The operation was achieved once for each voxel, label by label. The procedure was repeated until reaching a stabilisation of the dilatation process (≈15 iterations). After this sequence, either few voxels were not labelled or the voxels close to contact regions had two labels, as highlighted with the white voxels in the example shown in Fig. 3(d). In both cases, these voxels were associated with the main label of its 26-neighbours. The image obtained after this last operation is displayed in Fig. 3(e).

Hence, the described image treatment procedure provides a 3D image with labelled fibres. The numbers of fibre–fibre contacts N_c can thereafter be estimated by identifying the labels the fibres of which were in contact. It was also possible to obtain rough estimates of contact surfaces, by considering that a voxel belonged to a fibre–fibre contact surface if one of its 26-connex neighbouring voxels belonged to another fibre (a contact zone has thus a thickness of two voxels). A contact region between two connected fibres gathered all voxels of the contact zone between these fibres. As a consequence, it could be split into several voxel subsets, *i.e.* a contact zone can appear as a set of disconnected sub-surfaces.

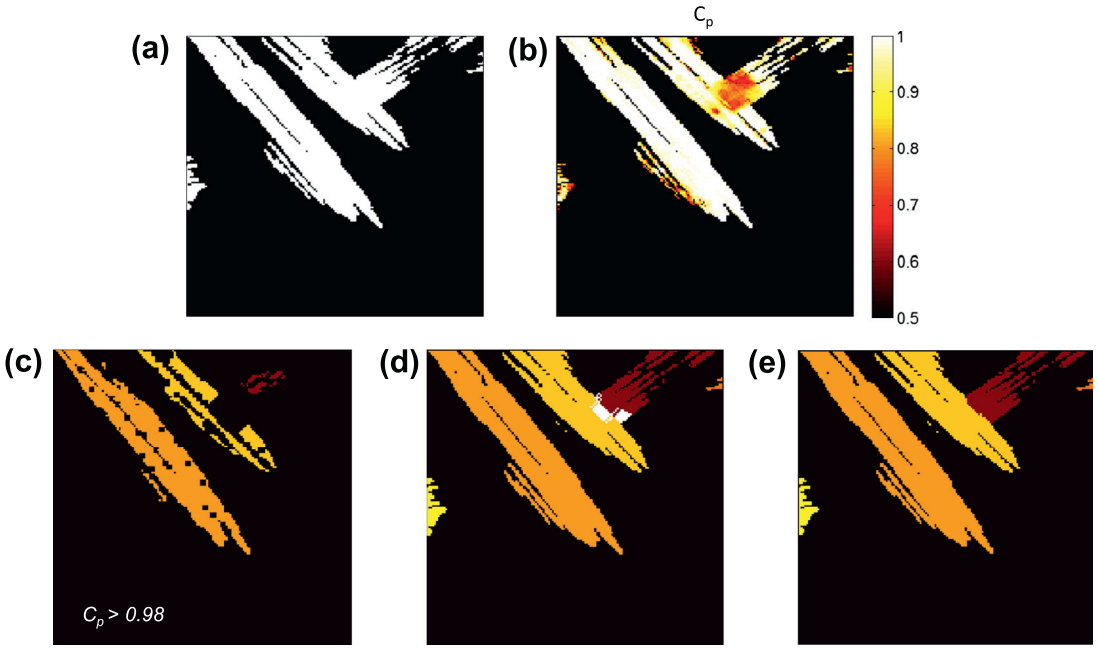

Fig. 3. (a) Slice along the ($\mathbf{e}_1$, $\mathbf{e}_2$) plane of a small segmented 3D image of a network of glass fibre bundles (160 × 160 × 100 voxels, 1 voxel = 18^3 μm^3), (b) map of the mean angular deviation C_p, (c) labelled image after thresholding of C_p, (d) image after the successive dilatations with a 2D elliptic structuring element and (e) image at the end of the identification procedure.

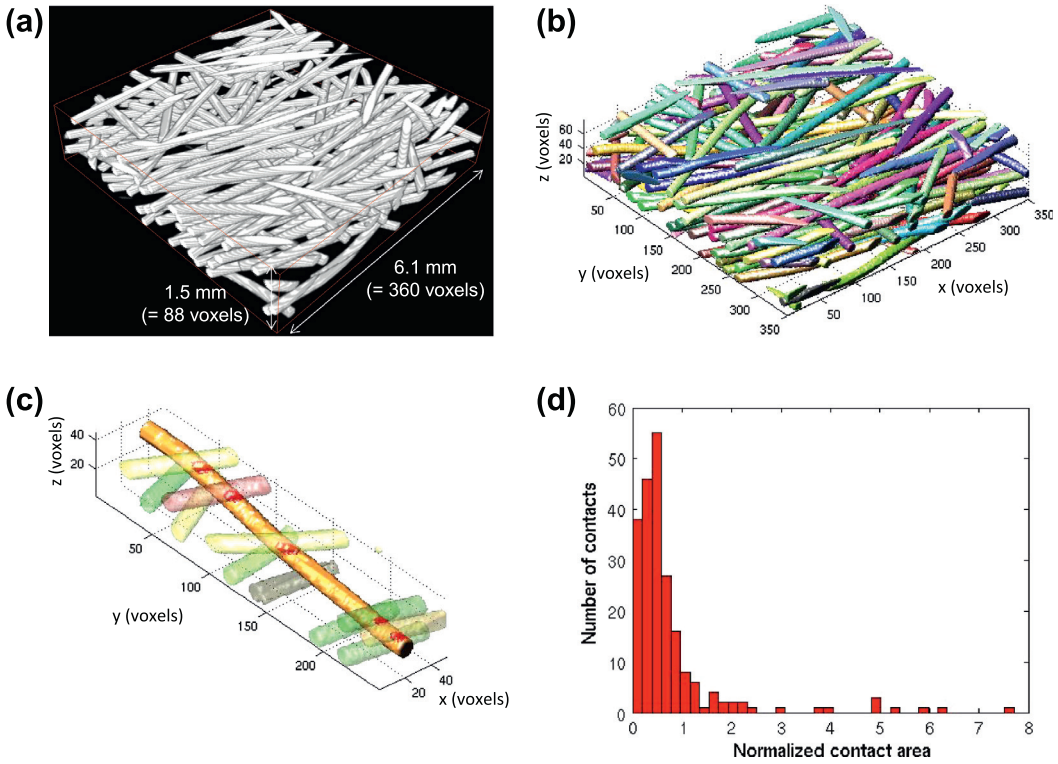

Fig. 4. (a) Original 3D image obtained by X-ray tomography of a network of copper fibres reinforcing a polymer composite (360 × 360 × 88 voxels, 1 voxel = 17^3 μm^3), (b) 3D image with labelled fibres after the identification procedure, (c) 3D image of fibre–fibre contact surfaces represented in red along a fibre extracted from the labelled image and (d) area distribution of fibre–fibre contacts. (For interpretation of the references to colour in this figure legend, the reader is referred to the web version of this article.)

4. Validation

Fig. 4(a) and 4(b) exhibit the original 3D image of the network of copper fibres and the same 3D image with coloured labelled fibres after the identification procedure, respectively. By visually inspecting the obtained image, the identification of fibres seems fairly accurate. It can be noticed that a negligible number of voxels was not correctly attributed (*i.e.* labelled differently from the fibre they belong to). This particularly occurred in zones where fibres were locally nearly parallel. As shown in the zoom of Fig. 4(c),

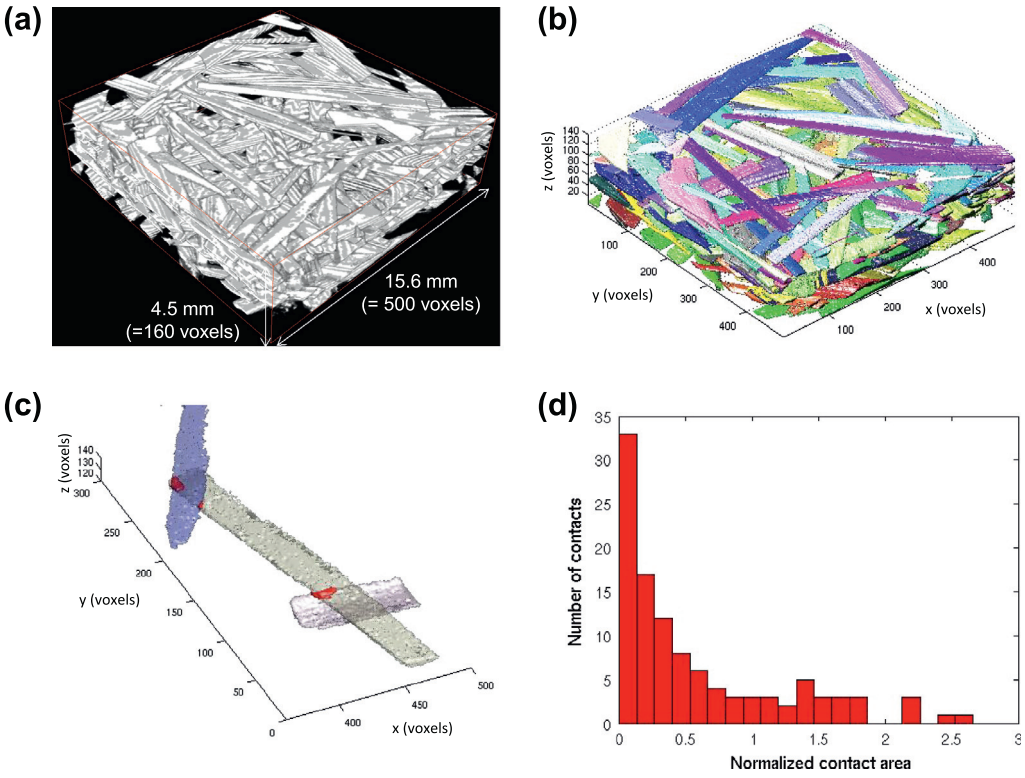

Fig. 5. (a) 3D image obtained by X-ray tomography of a network of glass fibre bundles reinforcing a polymer composite (500 × 500 × 146 voxels, 1 voxel = 31.2^3 μm^3), (b) 3D image with labelled bundles after the identification procedure, (c) same 3D image with fibre–fibre contact zones represented in red and (d) area distribution of fibre–fibre contacts. (For interpretation of the references to colour in this figure legend, the reader is referred to the web version of this article.)

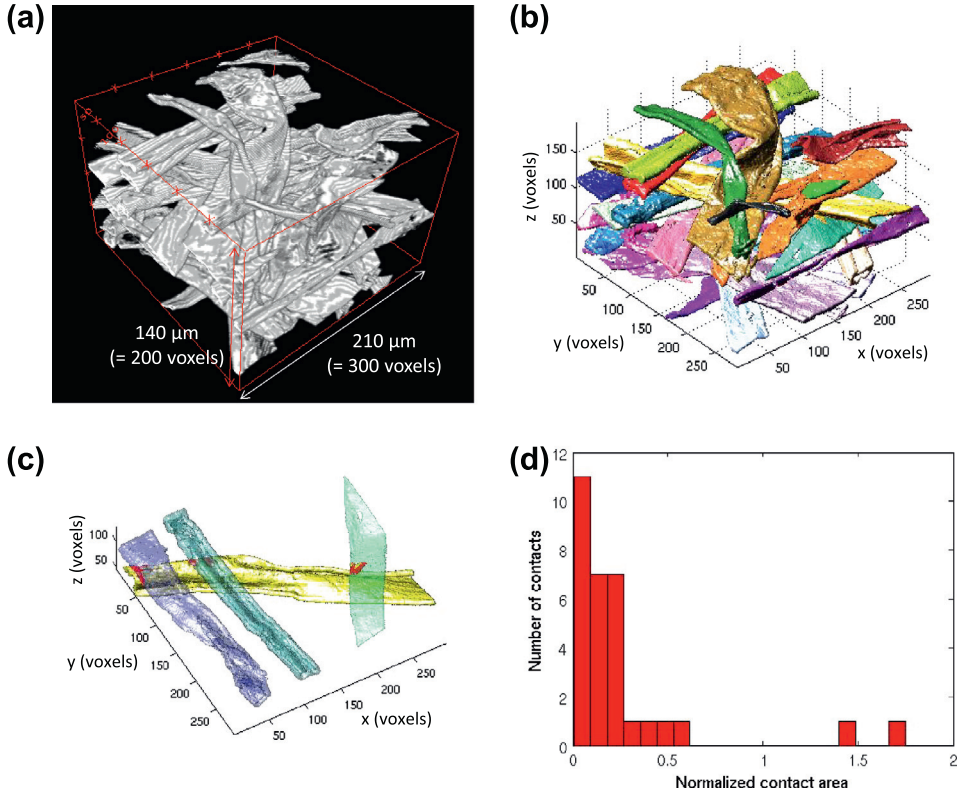

Fig. 6. (a) 3D image obtained by X-ray tomography of a network of cellulosic fibres obtained by a papermaking process (300 × 300 × 200 voxels, 1 voxel = 0.7^3 μm^3), (b) 3D image with labelled fibres after the identification procedure, (c) 3D image of fibre–fibre contact zones represented in red along a fibre extracted from the labelled image and (d) area distribution of fibre–fibre contacts. (For interpretation of the references to colour in this figure legend, the reader is referred to the web version of this article.)

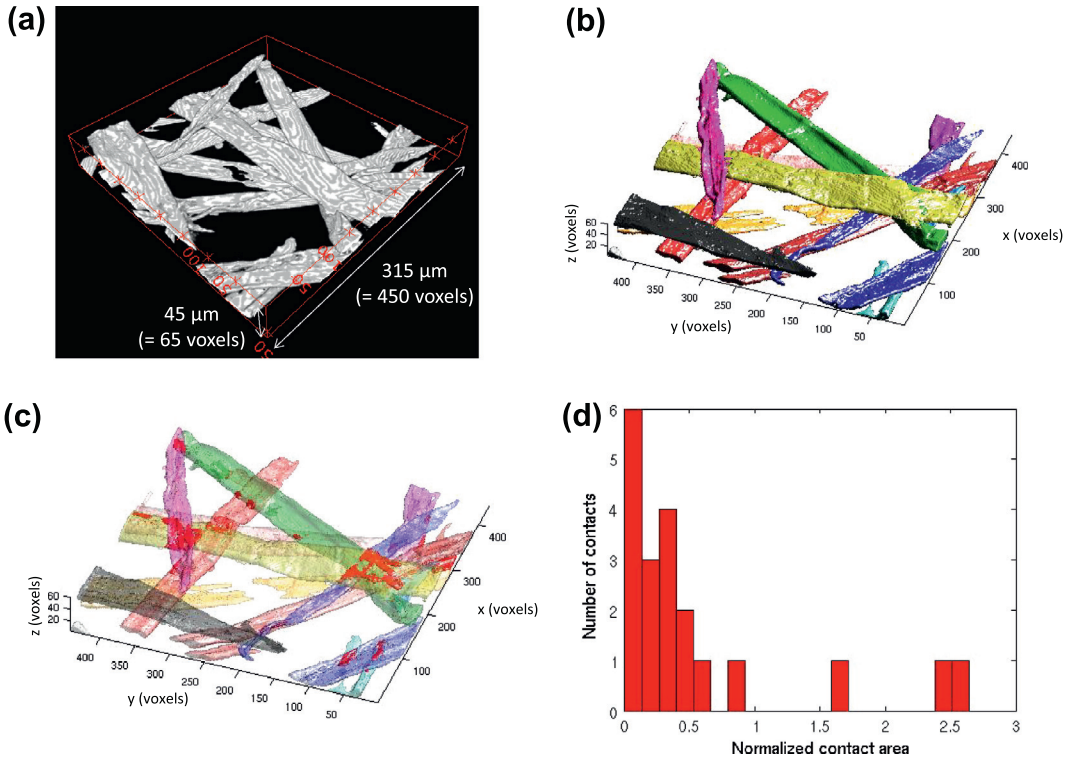

Fig. 7. (a) 3D image obtained by X-ray tomography of a network of cellulosic fibres obtained by a papermaking process (450 × 450 × 65 voxels, 1 voxel = 0.7^3 µm^3), (b) 3D image with labelled fibres after the identification procedure, (c) same 3D image with fibre–fibre contact zones represented in red and (d) area distribution of fibre–fibre contacts. (For interpretation of the references to colour in this figure legend, the reader is referred to the web version of this article.)

fibre–fibre contacts were also properly detected using the proposed algorithm. As revealed from Figs. 5–7, identical qualitative observations can be established for the network of glass fibre bundles (Figs. 5(a–c)), but also for the two tested networks of cellulosic fibres (see Figs. 6 and 7(a–c)). To further validate the method, more quantitative results could also be extracted from the analysis. They are briefly summarised and discussed below:

- For the network of copper fibres (Fig. 4), the total number of fibres is found to be $N_f = 133$. This estimation is equal to the number of fibres counted in Orgéas et al. [17] from either a manual detection of fibres or by a thresholding based on the 3D Euclidian distance map (see Section 2). Moreover, the measured number of fibre–fibre contacts reaches $N_c = 218$. This result is very close to the value of 214 assessed in Orgéas et al. [17] from an homotopic thinning followed by a 3D reconstruction of the fibrous microstructure (see Section 2). It can thus be concluded that, to identify cylindrical fibres with circular and constant cross-section and their contacts, the proposed procedure can fairly be considered as efficient as classical geometrical skeletonisation methods. The observed slight discrepancy may be attributed to a less accurate separation of parallel fibres in the case of the present method.
- As in the case of copper fibres, the identification of glass fibre bundles inside the fibrous media displayed in Fig. 5 is also accurate. Indeed, the number of labelled fibres is $N_f = 148$: it is equal to the number of fibres manually counted by Guiraud et al. [6] (see Section 2). Likewise, the estimated number of bundle-bundle contacts reaches $N_c = 108$. This value slightly differs from the value of 116 assessed by Guiraud et al. [6] (see Section 2). This difference may probably be attributed to the method proposed in Guiraud et al. [6]. Since the authors assumed constant elliptical cross section of the bundles in order to detect bundle-bundle contacts, their method could yield to erroneous estimation of N_c. Conversely, the identification procedure here proposed does not take into account such a strong hypothesis and can hence handle fibres with flat but also variable cross sections.
- A similar quantitative analysis was also carried out with the two cellulosic fibrous networks depicted in Figs. 6 and 7. The number of fibres N_f was respectively estimated to 30 and 15. Such estimations exactly fit those that were obtained from a manual fibre picking. Furthermore, the number of fibre–fibre contacts N_c was found to reach 32 and 18, respectively. Here again, these results are very close to those assessed from a manual observations of the considered images, i.e. 32 ± 1 and 18, respectively.

Thus, by performing an appropriate finding and labelling of fibres and their contacts inside a 3D segmented image with reasonable computation time (calculations for the analysed volumes approximately lasted 10 h on a standard workstation), the proposed method constitutes a first and required step to carry out a deeper analysis of the fibre morphologies and geometries: positions, local orientations, curvatures and twists of the fibre centrelines [9], shape and orientation of the fibre cross sections. It can also bring useful information about the position, orientation, morphology and the geometry of fibre–fibre contacts. For instance, contact orientation tensors built from the normal of each mean contact plane could be estimated [9,6,17]. Similarly, graphs (c–d) shown in Figs. 4–7 also illustrated some of the useful and original information that could be extracted about the morphology and the geometry of contacts:

- As evidenced from the graphs (c) in these figures, fibre–fibre contacts display various morphologies depending on the complexity of the fibre geometry: single contact surfaces or contact

zones with multiple sub-surfaces. The first type of morphologies are the most observed in the case of fibres with simple and convex cross sections (see Fig. 4(c)), whereas the first and the second morphologies can be encountered if the fibres cross sections become more complex, as in the case of the glass fibre bundles or the wood fibres (see Figs. 5-7(c)).

- The graphs (d) in these figures also provide the distributions of the estimated areas of contact zones inside the scanned volumes. On each of these graphs, the areas were normalised by a characteristic contact surface area which corresponds to the square of the mean principal width of the considered fibres or fibre bundles:
  - Whatever the considered fibrous microstructure, the median value of the normalised contact surface area is always below 1: it is equal to 0.48, 0.38, 0.19 and 0.37 for the fibrous microstructures shown in Figs. 4–7, respectively.
  - For the fibrous media with planar random fibre orientation, *i.e.* for fibrous media plotted in Figs. 5–7, the normalised contact surface areas range between 0 and 3. Conversely, for the copper fibrous media (Fig. 4), the contact area distribution is wider: this is related to the preferred fibre orientation along one direction that yields to increase contact surfaces between fibres [22,9].
  - The influence of processing conditions on contact surfaces can also be clearly highlighted: as evident from the graphs in Figs. 6 and 7(d), the higher the pressure during the paper processing, the larger the fibre–fibre contact surface areas.

Contact surfaces often play a critical role on the macroscale physical properties of fibrous networks. As a consequence, having an automatic access to their number, position, morphology and geometry may significantly contribute to the understanding and modelling of these properties.

5. Concluding remarks

In this work, we have proposed a novel method to identify and label fibres with complex anisotropic cross sections together with their contacts within 3D images of disordered fibrous materials. The method relies upon a fine analysis of the local orientation map obtained from the 3D directional distance map. The reliability of the method was proved for real networks with slightly wavy fibres exhibiting simple (circular) or very complex cross sections (with variable irregular and slender shapes that could also be twisted along the fibre centrelines).

- The thresholding operation based on the local and intrinsic angular deviation parameter C_p that is directly deduced from the 3D directional distance map seems to be relevant for the considered fibrous materials and their associated 3D images, *i.e.* (i) for images that had rather low spatial resolutions (down to only 3–5 voxels along the smallest thickness of the fibres), (ii) for low to moderate fibre contents, and (iii) for slightly wavy fibres that were not (nearly) parallel. At such spatial resolutions, fibre contents and orientations, it is expected to be still efficient for more tortuous fibres. Other existing solutions can be used to tackle the case of (nearly) parallel fibres, for which the proposed method is inappropriate.
- The dilatation operation that follows the C_p thresholding is another key point of the method. Its efficiency and accuracy greatly depends on the shape, the dimensions and the orientation of the selected structuring element. In this work, for the sake of simplicity, the dilatation operation was successfully performed using a unique structuring element whose orientation was set as a function of the mean orientation of each fibre. However, in view of treating highly tortuous fibres and improving the identification accuracy in contact zones, the shape, dimensions and orientation of the structuring element should be continuously adapted by using the local fibre information.

The automatic identification of fibres with complex anisotropic cross sections together with their contacts inside 3D images of disordered fibrous networks is the first requirement to obtain quantitative microstructural data on the morphologies and geometries of fibres and fibre–fibre contacts. If further studies are still required to improve this identification, the method proposed in this paper demonstrates that such valuable data are now accessible. If the 3D images were obtained from fibrous materials subjected to macroscale physical or mechanical loading, the evolution of the underlying deformation micro-mechanisms of the fibres and the fibre–fibre contacts could be better assessed.

Acknowledgements

This work was performed within the ANR research program "3D discrete analysis of deformation micromechanisms in highly concentrated fiber suspensions" (ANAFIB, ANR-09-JCJC-0030-01), the ESRF Long Term Project "Heterogeneous Fibrous Materials" (exp. MA127). J. Viguié also thanks Grenoble INP together with the PowerBonds and WoodWisdom ERA-NET project for his research grant.

References

[1] Altendorf H, Jeulin D. 3D directional mathematical morphology for analysis of fiber orientations. Image Anal Stereol 2009;28:143–53.
[2] Axelsson M. 3D tracking of cellulose fibres in volume images. Proc Int Conf Image Process 2007;4:309–12.
[3] Axelsson M. Estimating 3D fibre orientation in volume images. Pattern Recognition. Proc Int Conf, Pattern Recognition; 2008. p. 1–4.
[4] Delisee C, Badel E, Lux J, Malvestio J. 3D microstructural characterization and local densification of cellulosic fibrous insulators under compression. Eur J Environ Civil Engine 2009;13:429–42.
[5] Eberhardt CN, Clarke AR. Automated reconstruction of curvilinear fibres from 3D dataset acquired by X-Ray Microtomography. J Microsc 2002;206:41–53.
[6] Guiraud O, Orgéas L, Dumont PJJ, Rolland du Roscoat S. Microstructure and deformation micromechanisms of concentrated fiber bundle suspensions: an analysis combining X-ray Microtomography and pull-out tests. J Rheol 2012;56:592.
[7] Hild F, Maire E, Roux S, Witz JF. Three-dimensional analysis of a compression test on stone wool. Acta Mater 2009;57:3310–20.
[8] Krause M, Hausherr JM, Burgeth B, Herrmann C, Krenkel W. Determination of the fibre orientation in composites using the structure tensor and local X-ray transform. J Mater Sci 2010;45:888–96.
[9] Latil P, Orgéas L, Geindreau C, Dumont PJJ, Rolland du Roscoat S. Towards the 3D in situ characterisation of deformation micro-mechanisms within a compressed bundle of fibres. Compos Sci Technol 2011;71:480–8.
[10] Le T-H, Dumont PJJ, Orgéas L, Favier D, Salvo LE, Boller E. X-ray phase contrast microtomography for the analysis of the fibrous microstructure of SMC composites. Composites Part A 2008;39:91–103.
[11] Lux J, Delisée C, Thibault X. 3D characterisation of wood based fibrous materials: an application. Image Anal Stereol 2006;25:25–35.
[12] Lux J. Automatic segmentation and structural characterization of low density fibreboards. Image Anal Stereol 2013;32:13–25.
[13] Malmberg F, Lindblad J, Östlund C, Almgren KM, Gamstedt EK. Nucl Instrum Methods Phys Res, Sect A 2011;637:143–8.
[14] Marulier C, Dumont PJJ, Orgéas L, Caillerie D, Rolland du Roscoat S. Towards 3D analysis of pulp fibre networks at the fibre and at the bond levels. Nord Pulp Pap Res J 2012;28:245–55.
[15] Masse JP, Salvo L, Rodney D, Bréchet Y, Bouaziz O. Influence of relative density on the architecture and mechanical behaviour of a steel metallic wool. Scripta Mater 2006;54:1379–83.
[16] Palágyi K, Kuba A. A 3D 6-subiteration thinning algorithm for extracting medial lines. Pattern Recognit Lett 1998;19:613–27.
[17] Orgéas L, Dumont PJJ, Vassal JP, Guiraud O, Michaud V, Favier D. In-plane conduction of polymer composite plates reinforced with architectured networks of Copper fibres. J Mater Sci 2012;47:2932–42.
[18] Rolland du Roscoat S, Decain M, Thibault X, Geindreau C, Bloch JF. Estimation of microstructural properties from synchrotron X-ray microtomography and determination of the REV in paper materials. Acta Mater 2007;55:2841–50.
[19] Sandau K, Ohser J. The chord length transform and the segmentation of crossing fibres. J Microsc 2007;226:43–53.

[20] Svensson S, Aronsson M. Using distance transform based algorithms for extracting measures of the fibre network in volume images of paper. IEEE Trans Syst Man Cyber-Part B 2003;33:562–71.
[21] Tan JC, Elliott JA, Clyne TW. Analysis of tomography images of bonded fibre networks to measure distributions of fibre segment length and fibre orientation. Adv Eng Mater 2006;8:495–500.
[22] Toll S. Note on the tube model. J Rheol 1993;37:123–5.
[23] Viguie J, Dumont PJJ, Mauret E, Rolland du Roscoat S, Vacher P, Desloges I, Bloch JF. Analysis of the hygroexpansion of a lignocellulosic fibrous material by digital correlation of images obtained by X-ray synchrotron microtomography: application to a folding box board. J Mater Sci 2011;46:4756–69.
[24] Walther T, Terzic K, Donath T, Meine H, Beckman F, Thoemen H. Microstructural analysis of lignocellulosic fiber networks. Dev X-ray Tomogr V 2006:6318.
[25] Wernersson LG, Brun A, Luengo Hendricks CL. Segmentation of wood fibres in 3D CT images using graph cuts. Lecture Notes Comput Sci 2009;5716:92–102.
[26] Yang H, Lindquist BW. Three-dimensional image analysis of fibrous materials. Proc Appl Dig Image Process XXIII 2000:4115.